Cleaner Materials 20 (2026) 100397

Contents lists available at ScienceDirect

Cleaner Materials

journal homepage: www.journals.elsevier.com/cleaner-materials

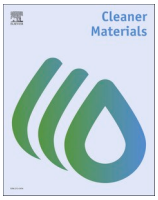

Utilization of waste plastic for plasma-assisted deposition of carbon nanowalls on electrodes for sustainable high-performance energy-storage devices

Alenka Vesel [a,*], Gregor Primc [a], Miran Mozetič [a], Melita Tramšek [b], Evelin Gruden [b], Haojie Fei [c], Peter Saha [c], Marian Lehocky [c], Rok Zaplotnik [a]

[a] Department of Surface Engineering, Jozef Stefan Institute, Jamova cesta 39, 1000 Ljubljana, Slovenia
[b] Department of Inorganic Chemistry and Technology, Jozef Stefan Institute, Jamova cesta 39, 1000 Ljubljana, Slovenia
[c] Centre of Polymer Systems, Tomas Bata University in Zlín, Tr. T. Bati 5678, 76001 Zlín, Czech Republic

ARTICLE INFO

Keywords:
PECVD synthesis
Carbonnanowalls
Graphene-like sheets
Electrode material
Supercapacitors
Plastic material reuse

ABSTRACT

Current global policies, such as circular economy, electrification, and low carbon footprint dictate the replacement of fossil fuels for synthesizing electrodes of graphene supercapacitors with renewable sources. The traditional method for depositing graphene and similar structures is based on gaseous hydrocarbons. The possibility of replacing them with waste plastic is presented. We used propane and waste plastics (mostly polypropylene) for the deposition of a few μm-thick deposit of carbon nanowalls composed of vertically oriented multilayer graphene-like sheets on electrodes by plasma-enhanced chemical vapor deposition (PECVD). We studied their morphology and structure, as well as the performance of coin-shaped supercapacitors. The graphene-like coatings were deposited in plasma sustained at the pressure of 16 Pa by inductively coupled RF discharge in the H mode at the forward power of 500 W and power density approximately $8x10^6$ W/m^3. Such a powerful plasma caused thermal decomposition of the waste plastic. Optical emission spectroscopy showed significant differences only within the first few seconds of plasma treatment, which was enough to supply precursors for graphene growth. Both scanning and transmission electron microscopies showed similar structures for deposits prepared from propane or waste plastic, and the deposition rates of roughly 100 nm/s were observed. Waste plastic enabled the deposition of 2–3 times densely packed multilayer graphene-like sheets of a typical thickness of 5 nm at deposition times over 1 min. Raman spectroscopy indicated a somewhat lower concentration of defects for samples deposited from polypropylene, but the I_D/I_G versus the average distance between the neighboring multilayer graphene-like sheets followed the same line. The specific capacitance increased steeply with deposition time for deposits prepared from waste plastic and it was found to be linearly dependent on the ratio between the effective and projected areas of both precursors. The capacitance versus the I_D/I_G followed the same curve for both precursors. The results demonstrate the feasibility of replacing gaseous hydrocarbons with waste plastics for PECVD deposition of graphene electrodes.

1. Introduction

Carbon nanomaterials are suitable coatings on electrodes in energy storage devices like batteries and supercapacitors, which are increasingly important for sustainable energy solutions. They have some superior properties, e.g., high specific surface area and appropriate electrical conductivity (Maduraiveeran and Jin, 2021). Since carbon is chemically inert, it is not prone to collapse or degradation of active materials caused by instability at the electrode/electrolyte interface (Zhao et al., 2024). Carbon nanomaterials have various morphologies, including fullerenes (zero-dimensional (0D) carbon), carbon nanotubes and nanowires (one-dimensional (1D) carbon), and graphene (two-dimensional (2D) carbon) (Maduraiveeran and Jin, 2021). Another type of carbon nanomaterial is carbon nanowalls (CNW). CNW are composed of vertically oriented graphene-like sheets (Hori et al., 2011; Shiji et al., 2005; Kondo et al., 2009) and are thus, because of their 3D carbon network, classified as three-dimensional carbon materials. Vertically oriented graphene sheets exhibit additional beneficial properties

* Corresponding author.
E-mail address: alenka.vesel@ijs.si (A. Vesel).

https://doi.org/10.1016/j.clema.2026.100397
Received 1 September 2025; Received in revised form 15 April 2026; Accepted 15 April 2026
Available online 17 April 2026

compared to horizontal 2D graphene layers. By changing the orientation of graphene sheets from horizontal to vertical, their electronic band structure and bandgap can be controlled, and the surface area can be increased (Sahoo et al., 2022). Furthermore, because of their wall-like morphology, CNWs have a high density of sharp edges with defects, which is important for higher charge storage capacity (Yen et al., 2015; Zhou et al., 2018; Kim et al., 2015). The thickness of the walls is usually a few nanometers (Hiramatsu et al., 2013). However, their length and height can be several microns, depending on the deposition technique, gas precursor, and growth time (Denysenko et al., 2020; Yerlanuly et al., 2021). Individual vertically aligned nanowalls can be well separated or interconnected, forming a dense mesh-like structure (Kondo et al., 2009; Vesel et al., 2021). Thus, the performance of supercapacitors made of CNW electrodes will depend on the orientation, density, size, and arrangement of the graphene walls. The energy and power densities of supercapacitors depend on the active surface area of the deposited nanocarbon and its electrical conductivity, which influence charging and discharging at the electrode–electrolyte interface (Sahoo et al., 2022). Carbon-based electrodes are usually used in electrochemical double-layer capacitors (EDLC), where energy is stored through reversible electrostatic charge separation at the electrode–electrolyte interface, forming an electrical double layer (Sahoo et al., 2022).

Vertically oriented graphene walls could be synthesized by various methods. A comprehensive review of reported methods was published recently (Wu et al., 2024). CNWs are often synthesized by chemical vapor deposition (CVD) from methane or acetylene at high temperatures and in the presence of a catalyst (Shimabukuro et al., 2008; Itoh et al., 2006; Manawi et al., 2018). Another technique is plasma-enhanced chemical vapor deposition (PECVD), in which plasma is used to partially decompose carbon-containing gaseous precursors and generate reactive radicals that serve as building blocks for deposited CNWs (Vesel et al., 2019; Cui et al., 2015; Vizireanu et al., 2012). Plasma sustained by direct current (DC), microwave (MW), and radiofrequency (RF) (capacitive and inductive) discharges has been used for CNW synthesis (Meško et al., 2012; Kim et al., 2015; Yerlanuly et al., 2021; Ghosh et al., 2017). Changing discharge parameters (power, frequency, gas pressure and flow, plasma to substrate distance, and temperature) enables the manipulation of the morphology of CNW (Zeng and Lin, 2014; Vesel et al., 2019; Shiji et al., 2005; Zhang et al., 2019; Cui et al., 2015; Lehmann et al., 2016; Gentoiu et al., 2017; Sahoo et al., 2022; Ghosh et al., 2017). PECVD can be performed using different gases like methane and acetylene, which are often mixed with hydrogen and argon (Shiji et al., 2005; Teii et al., 2009; Kondo et al., 2009).

Another important factor influencing supercapacitor behavior is the wettability of the deposited nanomaterial. Good wettability is important for complete wetting, thus enabling better electrolyte–electrode interactions by providing a high contact area and also influencing ions' mobility and their entering the space between the walls (Wu, 2022; Largeot et al., 2008; Kim et al., 2004; Heimböckel et al., 2019). The surface of as-deposited CNWs is hydrophobic. The water contact angle can be as high as 130° (Paul et al., 2024). However, the hydrophilicity can be modified by plasma treatment. Even a brief (less than 1 s) treatment with oxygen plasma caused CNW samples to become superhydrophilic (Paul et al., 2024). Sahoo et al. obtained a superhydrophilic surface by in-situ post-deposition oxygen plasma treatment (Sahoo et al., 2018). They found a correlation between wettability and capacitance. For the superhydrophilic surface functionalized with OH groups, 10 times enhanced capacitance was observed. Similarly, Deheryan et al. (2014) synthesized CNW with water contact angles of 16 and 141° and found corresponding capacitances of 922 and 167 μF/cm^2, respectively. Furthermore, electrochemically active surface oxygen-containing functional groups have a significant effect on capacitance because they can undergo charge-transfer reactions in electrolytes (Zuliani et al., 2018). Zuliani et al. (2018) showed that porous carbon that contained oxygen had a capacitance of 12.2 μF/cm^2, while the capacitance of an oxygen-free sample was 8.8 μF/cm^2. They showed that carboxyl and phenol groups contributed approximately 1.1 μF/cm^2.

Plasma deposition enables rapid growth of CNW deposits. A deposition rate of 0.1 μm/s can be obtained, which makes the technique attractive for industrial applications (Vesel et al., 2022; Vesel et al., 2021). Furthermore, CNWs can be deposited by using solid carbon-based precursors like various polymer materials in combination with hydrogen, oxygen, or nitrogen plasma (Vesel et al., 2022). CNWs could thus be synthesized from waste plastic materials, which makes them even more interesting, as this plasma-deposition process is in line with the circular economy policy.

In this paper, we report the deposition kinetics and structure of CNWs grown by PECVD from two different precursors, i.e., propane (C_3H_8) or polypropylene (PP). The polymer PP was used to demonstrate the possibility of recycling polymers to produce high-quality electrodes. Electrodes with CNW deposited under different conditions were used to assemble capacitors. Their capacitance was measured and correlated with their structure.

2. Experimental

2.1. Carbon nanowall deposition

Carbon nanowalls were deposited in an inductively coupled radio-frequency plasma system (ICP), schematically presented in Fig. 1. The plasma reactor consisted of a discharge borosilicate tube with an inner diameter of 3.6 cm and a length of 75 cm. A coil with 6 turns was mounted around the discharge tube and connected to a radio-frequency (RF) generator (CESAR 1310 Advanced Energy) through a matching network (ICP VarioMatch Advanced Energy). The discharge tube was pumped with a two-stage rotary pump (Edwards E2M80) with a nominal pumping speed of 80 m^3/h. The pressure was measured with an absolute pressure gauge (MKS Baratron Type 722A). Hydrogen with 99.999% purity or propane with > 96% purity (the rest were other hydrocarbons) were leaked in the discharge tube through mass flow controllers (Advanced Energy Aera FC-7700) or a dosing needle valve.

Stainless steel coin cell battery spacer discs 15.8 mm in diameter and 0.5 mm thick were used as sample substrates. The substrates were cleaned with ethanol before being assembled into the plasma reactor. They were placed in the middle of the coil on a quartz holder, as seen in Fig. 1. CNWs were deposited using two carbon-containing precursors, i.e., propane and polypropylene. Hydrogen was introduced into the plasma reactor in the latter case to ensure stable discharge.

One precursor for CNW growth was propane (C_3H_8). The pressure in the plasma reactor was set to 16 Pa, the RF power was 500 W, and the deposition time was varied from 30 to 600 s. The second precursor was polypropylene (PP) foil provided by Goodfellow, which was exposed to hydrogen plasma (hereafter PP + H_2). The empirical PP formula is $(C_2H_4)_n$. Pieces of PP with masses of 200 mg were assembled in the plasma reactor a few centimeters upstream from the stainless-steel disk substrate, as shown in Fig. 1. Fresh PP foils were used for each

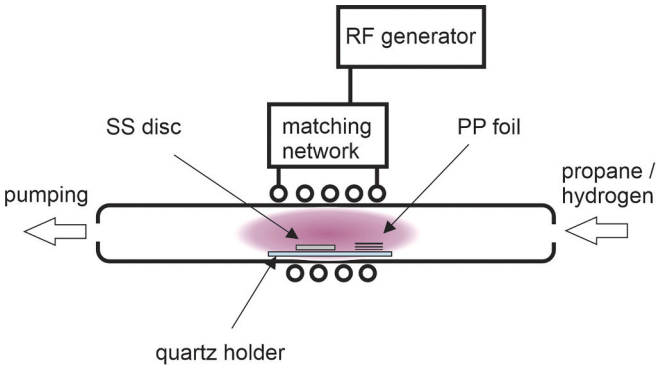

Fig. 1. Plasma setup for deposition of CNW.

deposition. Hydrogen plasma at 16 Pa and 500 W was used in this case. Hydrogen plasma caused the melting of PP and the formation of radicals that served as building blocks for CNW. The deposition time when using PP + H_2 varied between 30 and 120 s. The longest deposition time for the PP + H_2 was thus shorter than for propane, as propane was uniformly and continuously supplied to the plasma system, whereas the PP polymer gradually degraded and eventually ran out after 120 s. In later experiments, the PP amount was increased to allow longer deposition times. These conditions were applied only for selected additional characterizations. CNWs were deposited on stainless steel discs in triplicates. Each stainless-steel disc with CNW was deposited separately, and in between the depositions, the plasma reactor was cleaned with oxygen plasma to remove any deposits on the chamber walls that might influence the deposition kinetics.

The substrate temperature was monitored during deposition. Due to RF interference (the sample being positioned inside the coil), continuous recording was not reliable; therefore, the temperature evolution was estimated. In propane plasma, the temperature increased for approximately 1 min before stabilizing at approximately 720 °C, while in the PP + H_2 plasma it reached a stable value of approximately 820 °C after about 30 s.

Optical emission spectrometer (OES) Avaspec 3648 (Avantes, Netherlands) was used to monitor the plasma radiation during CNW deposition. The collimating lens connected to the optical fiber was positioned near the middle of the excitation coil. Optical emission spectra were measured in the range from 200 to 1100 nm with 0.3 nm resolution. Integration time was set to 1 ms.

2.3. Characterization of carbon nanowalls

2.3.1. Scanning electron microscopy (SEM) characterization

SEM micrographs were captured using the Thermo Fischer Scientific Verios 4G HP (USA) scanning electron microscope with Schottky field emission gun (FEG) source in secondary-electron mode. Samples were scanned in both field-free and immersion modes. In the immersion mode, the resolution is optimized by focusing the electron beam more tightly, which is ideal for capturing high-resolution images of nano-scale features. Samples were scanned at an accelerating voltage of 5 kV and a beam current of 25 pA. No conductive coating on the samples' surface was deposited before SEM analyses because of the adequate conductivity. The microscope was operated in immersion mode, and an in-lens (in-column) through-the-lens detector (TLD) was used.

2.3.2. Transmission electron spectroscopy (TEM) characterization

To check whether there are any significant orientational and structural differences between CNWs growth at different parameters, a transmission electron microscope Jeol JEM-2100 WITH Gatan CCD camera (Japan) was utilized. This instrument operated at an accelerating voltage of 600 kV and a beam current of 130 pA. These conditions were selected to optimize the resolution and contrast of the images while minimizing potential beam-induced damage to the samples. Plasma-prepared CNW samples were gently scratched from the substrate's surface and collected onto a lacey carbon TEM support film (200 copper mesh, Micro to Nano).

2.3.3. X-ray photoelectron spectroscopy (XPS) investigation

The samples were characterized by X-ray photoelectron spectroscopy (XPS). An XPS instrument model PHI Genesis, from ULVAC-PHI (Physical Electronics Ltd., Munich, Germany), was used. The base pressure in the XPS analysis chamber was 5×10^{-7} Pa. The samples were fixed to the sample holder with a double-sided copper tape. They were excited with X-rays over a spot with a diameter of 300 μm using monochromatic Al $K\alpha_{1,2}$ radiation with a photon energy of 1486.6 eV, generated at an operating voltage of 15 kV and a power of 30 W. The energy resolution as measured on the Ag $3d_5/_2$ peak was 0.6 eV. Photoelectrons were detected using a hemispherical analyzer operating in fixed analyzer transmission (FAT) mode. The analyzer was positioned at an angle of 45° with respect to the normal of the sample's surface. Survey scan spectra were acquired at a pass energy of 224 eV and an energy step of 0.4 eV, whereas high-resolution spectra were acquired at a pass energy of 27 eV and 0.1 ev energy step. The measurements were taken on two different spots on the surface of each sample. The XPS spectrometer is equipped with a dual electron–ion beam neutralization system for charge compensation; however, since our samples were conductive, only the electron beam was used. Binding energies were referenced to the C 1 s peak corresponding to sp^2-hybridized carbon (C=C) in CNWs, set to 284.4 eV, which is characteristic of graphitic/graphene-like carbon. The measured spectra were evaluated using the Multipak software (version 9.9.1.1) from Ulvac (Kanagawa, Japan), which was supplied together with the spectrometer. The asymmetry of the C1s spectrum of CNW, typical for sp^2-hybridized carbon, was confirmed by comparison with a reference sample of highly oriented pyrolytic graphite (HOPG).

2.3.4. Raman spectroscopy characterization

Raman spectra of the CNW deposits were recorded on a HORIBA JOBIN YVON LabRam-HR spectrometer equipped with the Olympus BXFM-ILHS microscope. Samples were excited by the 532 nm emission line (green) of a diode-pumped solid-state (DPSS) laser. The power of the laser was approximately 24 mW at the source and 14 mW at the sample. The exposition time was 20 s, and the spectra were accumulated 50 times.

2.3.5. Contact angle measurements

Contact angles of $TEABF_4$ electrolyte solution were measured to verify the wettability of the CNW electrodes by the electrolyte. This was performed using the Drop Shape Analyser DSA 100 (Krüss GmbH, Hamburg, Germany). A static contact angle was measured using a sessile drop method. The volume of a water drop was set to 2 μL. The images of the water drops were acquired by the software Advance (version 1.19.1.16401, from Krüss GmbH, Hamburg, Germany). The same software was also used to analyze images and determine the contact angles.

2.4. Assembling coin cells and electrochemical measurements

As explained above, samples were deposited in triplicate. One deposited sample was used for surface analysis, while the other two served as electrodes in a symmetric supercapacitor assembled in a CR2032 coin cell. A glass fiber filter membrane (Whatman, GF/A) was employed as the separator, and 1 M tetraethylammonium tetrafluoroborate/acetonitrile ($TEABF_4$/ACN) was used as the organic electrolyte. The cyclic voltammetry (CV) and electrochemical impedance spectroscopy (EIS) measurements of the assembled supercapacitors were conducted using an Autolab PGSTAT 128 N potentiostat (Metrohm, Prague, Czech Republic). EIS was performed at 1.1 V over a frequency range of 0.1 Hz to 100 kHz, with an applied AC signal amplitude of 10 mV. Galvanostatic charge/discharge (GCD) analysis and cycle life testing were carried out using a BCS-810 battery cycler (BioLogic, Seyssinet-Pariset, France).

Based on the EIS results and assuming a series resistor–capacitor configuration for these symmetric EDLCs, the frequency-dependent specific capacitance of a single electrode (C_f) was calculated as:

$$c_f = \frac{1}{2\pi f Z'' A} \tag{1}$$

where f is the frequency, Z'' is the imaginary part of the impedance, and A is the geometric area of the electrode. Conversely, the device capacitance (C_d) was derived from galvanostatic curves at different current densities using:

$$C_d = \frac{It}{\Delta U} \tag{2}$$

where I is the discharge current, t is the discharge time, and ΔU represents the potential window excluding the IR drop. The areal capacitance of each device (C_A) was then calculated as:

$$C_A = \frac{C_d}{A} \quad (3)$$

2.5. Reproducibility and repeatability

A large number of deposits were prepared, and reproducibility was assessed through repeated measurements, especially using SEM. SEM analyses (including thickness, average distance, and related parameters) were performed multiple times on different deposits, showing good reproducibility. Raman measurements were also repeated at multiple locations, but on the same samples. In addition, capacitance measurements were independently performed by a second external provider, yielding very similar results to those reported in this work.

3. Results and discussion

3.1. Plasma characterization during CNW deposition

Two different precursors were used for the CNW growth – propane and polypropylene. These materials are similar in composition, but one is gaseous at ambient conditions and the other is solid. The precursor state might influence the plasma parameters, and the parameters should impact the growth of CNW. Therefore, we first characterized both plasmas to detect differences when using different precursors (C_3H_8 or PP + H_2). Plasma was monitored with optical emission spectroscopy (OES) during CNW deposition. Typical OES spectra for both precursors are presented in Fig. 2. Plasmas of both precursors emit similar spectra. The following spectral features are detected: hydrogen atom emission lines (H_α and H_β), H_2 Fulcher band, C_2 Swan emission bands, and CH emission band. The only difference is in the intensity of hydrogen atom emission lines H_α and H_β, which is more pronounced in the case of the PP precursor because of using hydrogen plasma. The similarity in spectra long after igniting the discharge may be logical because of the similar composition of both carbon precursors. However, there is a difference in the time evolution of some spectral features during deposition. This is presented in Fig. 3.

In the case of PP polymer in H_2 plasma, there are time variations in the intensity of H_α, C_2, and CH peaks (Fig. 3a). This is not the case for propane plasma, where signals are constant with the minor exception of H_α (Fig. 3b). The reason for variations in the intensity of H_α, C_2, and CH peaks in Fig. 3a is the fact that PP polymer must be heated first to start decomposing into radicals that act as building blocks for CNW growth

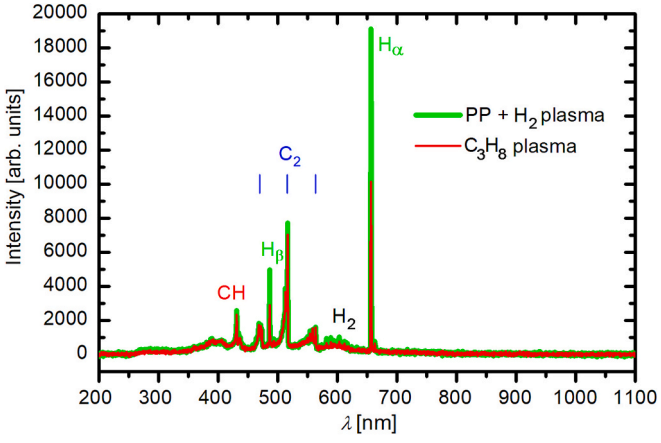

Fig. 2. Optical emission spectra of ICP plasma for C_3H_8 plasma and H_2 plasma with solid PP precursor 15 s after plasma ignition.

(Vesel et al., 2022). Fig. 3a reveals that it takes several seconds before the signal is stabilized after approximately 8 s. Fig. 4 shows the time variation of the ratio between the most intense hydrogen spectral features (H_α/H_β and H_α/H_2). The ratio H_α/H_β is identical (the blue curve overlaps the green curve), which indicates the same electron temperature in both plasmas. There are minor differences in the H_α/H_2 intensity, especially in the first 20 s. These differences are due to the heating of the PP precursor. There are two consequences of the PP heating. First, the PP precursor contains a small amount of water, which vaporizes upon heating. This water vapor is then dissociated into oxygen and hydrogen atoms. As the temperature continues to rise, thermal decomposition of the PP begins, leading to a sudden release of C_xH_y molecules, which provide an additional source of hydrogen atoms through dissociation. Once the stable conditions are established, the H_α/H_2 ratio of both precursors becomes similar. Therefore, OES (Figs. 2–4) indicates that the CNW deposition kinetics should be similar for both precursors, except during the first 5–10 s when the plastic is heated to start significant decomposition.

3.2. Characterization of bare CNW

3.2.1. Morphology and structure of bare CNW

Numerous CNW deposits were prepared using both precursors and different deposition times. The surface morphology of deposits was analyzed by SEM, and selected images are shown in Fig. 5. For both types of precursors, the morphology of CNW is similar, indicating a very similar growth mechanism. The density of CNWs, the shape of particular walls, and the thickness vary with the deposition time. At the lowest deposition time probed in these experiments (30 s), vertically oriented graphene-like sheets forming an individual carbon nanowall are observed with well-defined spaces between the neighboring sheets, as observed in the upper row of Fig. 5(a and b). When the deposition time increases, the walls become denser and interconnected until forming a rather dense mesh. The mass loading for different deposition parameters is shown in the Supplemental Table S1.

SEM results in Fig. 5 are further supported by TEM analysis. Fig. 6 shows selected TEM images of CNW deposited in either propane or PP + H_2. A homogeneous, highly oriented, and dense structure is observed. As already observed in SEM images (Fig. 5), TEM images also show that the CNW deposits are similar for both precursors regarding their structure.

SEM was also used to examine a cross-section of the CNW deposits and to determine the thickness of the deposited CNW film. The thickness versus the deposition time is shown in Fig. 7a. As expected, the thickness of the CNW film increases with the deposition time. Another observation is that both precursors lead to the same deposition rate because the curves practically overlap. The growth rate is somewhat larger up to the deposition time of 2 min. This observation suggests that the density of CNW deposits increases with the deposition time because the mass deposition rate at prolonged times is constant, as can be concluded from the constant OES intensity of spectral features of the plasma during the deposition.

SEM images were also used to determine the average distance between the adjacent CNWs on the surface and the sum of the perimeters of all CNWs on the surface. This was determined with the ImageJ software from SEM images acquired at a magnification of 20,000×. The average distance between adjacent CNWs versus the deposition time and the average perimeter of all CNWs on the surface versus the deposition time are presented in Fig. 7b. As the average distance between the CNW decreases with the deposition time, the perimeter of all CNWs on the surface increases. Here we should stress again that the perimeter term from here on is meant for the sum of all CNWs perimeters on the surface.

Based on the findings obtained from Figs. 5–7, we can propose the mechanism for the CNW growth. It is illustrated in Fig. 8a and consists of three phases. The first phase starts after the initial nucleation, which leads to the growth of sparse CNWs that are almost perfectly vertically oriented. In the second phase, the branching of CNW begins when new

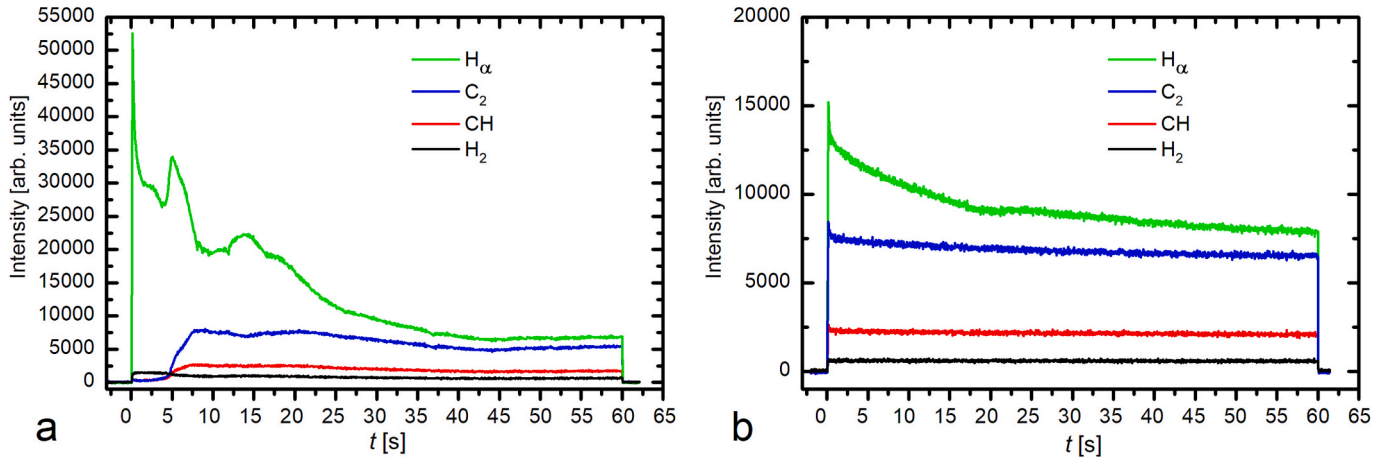

Fig. 3. Time evolution of different spectral features during CNW deposition with hydrogen plasma and PP precursor (a) and C_3H_8 plasma (b).

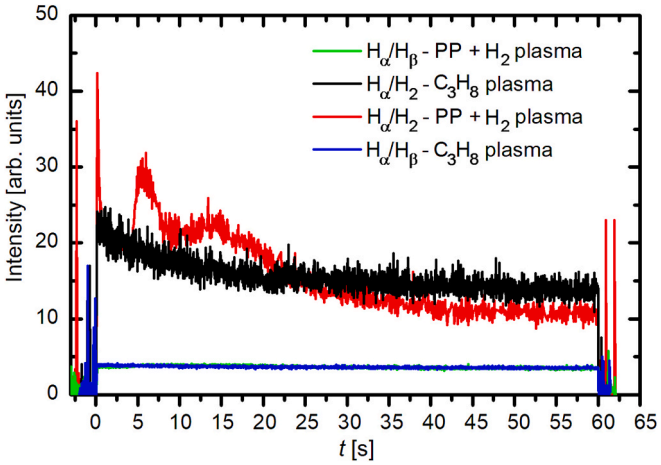

Fig. 4. Time evolution of ratios between some spectral features.

side carbon nanowalls start to grow on the existing nanowalls, which suppresses the growth rate of the CNW film and causes its densification. In the third phase, CNWs grow in all directions, not just vertically. The result of such non-directional growth is the formation of a much denser layer of CNW, so the slope of the growth curve in Fig. 7 decreases.

The cross-section of a deposited CNW film is shown in Fig. 8b. It supports the proposed growth mechanism. It shows a cross-section of a sample, which was treated by PECVD in hydrogen plasma with PP precursor for 1 min. Fig. 8b indicates that the flakes of CNW are sparse on the bottom of the CNW film and become denser somewhere in the middle, whereas the topmost structure is rather dense. The sparse structure occurs up to a thickness of a bit more than 1 μm, which corresponds to the treatment time of 30 s. Fig. 8b is therefore sound with Fig. 5 (first row), where the CNWs are well separated and grow practically only vertically.

The chemical composition and structure of the deposited CNW films were analyzed by XPS and Raman spectroscopy. XPS was used to check the purity of the deposits, particularly the presence of oxygen, which may affect the electrochemical performance of the electrodes. However, the XPS results indicate that oxygen is at the limit of detection. Examples of survey and high-resolution spectra are shown in Supplementary information (Figs. S1 and S2). Therefore, the influence of oxygen-containing surface functional groups on capacitance can be excluded in the present case.

The Raman spectra of selected CNW deposits are presented in Fig. 9. The deposition time is the parameter. The most intense band is the D band, which is related to the presence of defects and edges and is a typical band observed for CNWs (Yerlanuly et al., 2021; Haomin et al., 2006; Ni et al., 2006). As reported by Wang et al. (Haomin et al., 2006), the peak intensity ratio of D to G band (I_D/I_G) is strongly influenced by the edge length density of CNW, suggesting that the strong D band originates from the defects at the edges. Edge length density is defined as the average CNW length multiplied by the number density of the CNWs. The D band is followed by the G band, which is related to the graphitic-like structure (Yerlanuly et al., 2021; Davami et al., 2014; Zólyomi et al., 2011; Schuepfer et al., 2020). The G-band is related to the symmetry and vibrations of atoms within the hexagonal lattice due to sp^2-hybridized bonding and the delocalization of π-electrons (Zólyomi et al., 2011). The G band has a knee associated with the D' band. The latter is related to the finite size of crystals and edges of the graphene-like sheets (Vesel et al., 2020). Additionally, other bands are also observed, such as the second-order 2D band, D + G, and 2D' bands. The rather weak 2D band, as compared to the G band, indicates the multilayer graphene-like structure of the CNWs, because it is more intense than the G band of a single-layer graphene (Yoon and Cheong, 2012). This observation is supported by the TEM images shown in Fig. 6. The intensity of the peaks varies with the deposition time.

As already mentioned, an important factor in the characterization of carbon nanomaterials is the intensity (I – peak height was used) of the D and G bands. In fact, perfectly oriented graphite or graphene will have a negligible D band (Yoon and Cheong, 2012). Carbon materials with many defects will have a much higher D band than the G band and, therefore, a higher I_D/I_G ratio. The variation of I_D/I_G with the deposition time is shown in Fig. 10a. Fig. 10a shows that the I_D/I_G ratio decreases with the deposition time for both precursors, and it is more pronounced for PP + H_2 precursor. Similar findings were also found by Yerlanuly et al. (2021). The authors used the ICP-PECVD method for the deposition of CNW from the H_2/CH_4 precursor. They observed the decreasing intensity of I_D/I_G with the increasing growth time, which was related to the decrease in defects in the structure of CNW. In our case, the I_D/I_G variation correlates with the evolution of the CNW versus the deposition time observed on SEM images. At longer deposition times, when I_D/I_G ratio is smaller, the density of CNWs is higher. A decrease in the I_D/I_G ratio with the deposition time thus indicates that the number of defects is decreasing, although the density of CNW is higher. This can be explained by several factors. At shorter deposition times, there are larger individual walls with more exposed edges with defects (Fig. 5) that can contribute to a higher D signal. At longer deposition times, the specific edge area is smaller because edges are less exposed due to a denser structure, leading to a smaller D signal. The interconnection of edges also leads to greater continuity of walls and, consequently, fewer defects. Longer deposition times can also enable a higher probability of the

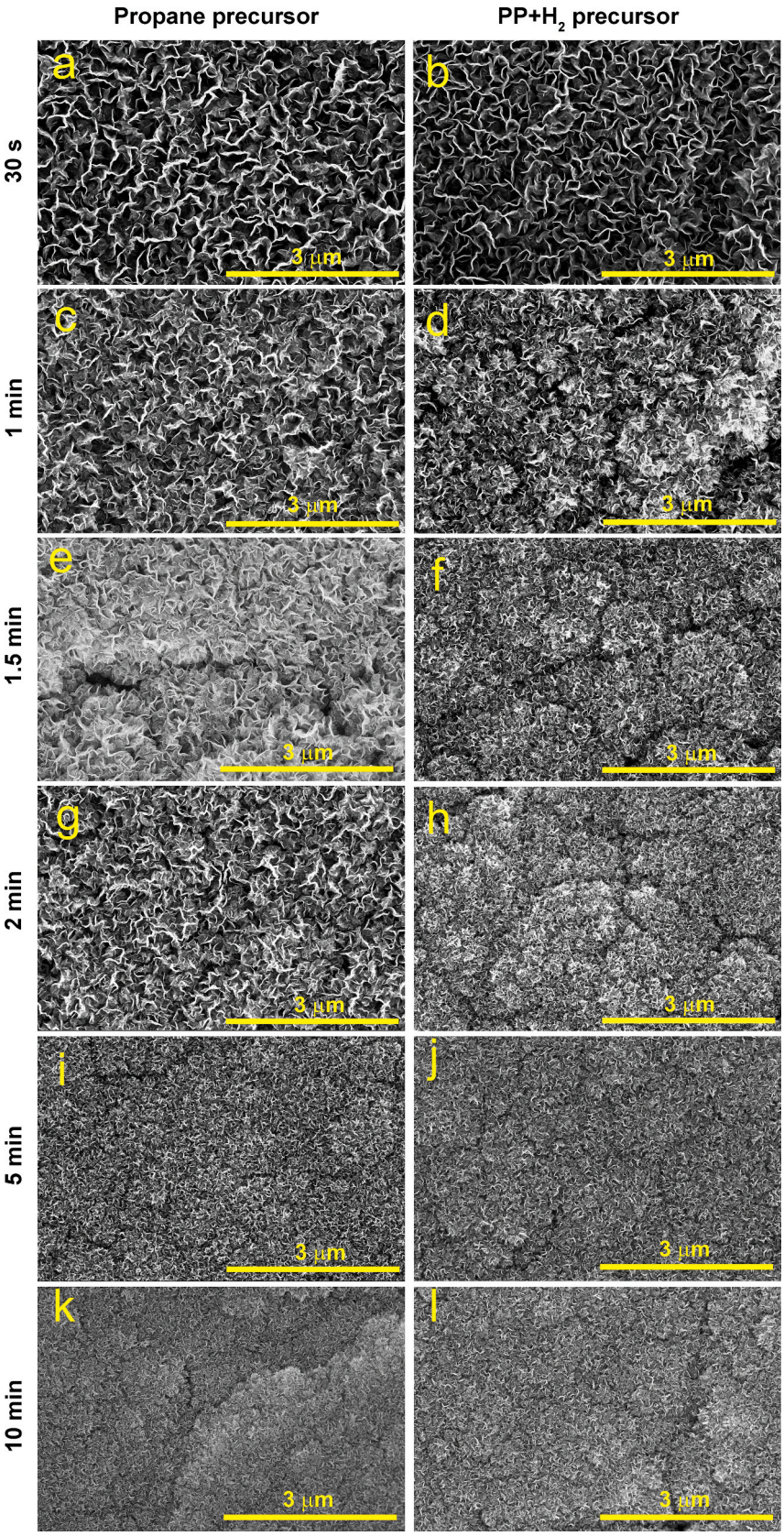

Fig. 5. SEM images of CNW deposited from propane or PP + H_2 precursor. The scale bar is 3 μm.

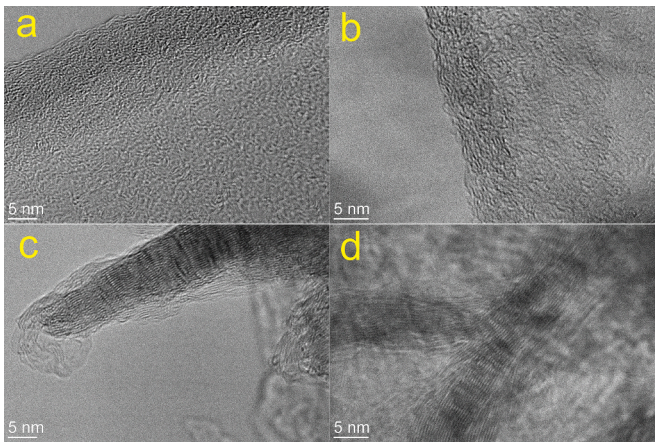

Fig. 6. TEM images of CNW deposited in 60 s using propane precursor (a and c) and PP + H_2 precursors (b and d).

healing of defects. Moreover, a denser structure can also cause edge shadowing and, consequently, a lower D signal.

Fig. 10b shows the I_D/I_G ratio as a function of the average distance between the CNWs, which was determined using SEM images. It can be seen that there is a linear correlation, indicating that the defects in the CNW are mainly due to the orientation of the flakes and thus to exposed edges and not to defects in the graphene-like sp^2 carbon lattice.

Additional information about the nature of defects can be obtained from the $I_D/I_{D'}$ ratio shown in Fig. 11. As already mentioned, the occurrence of a D peak is a general indicator of the presence of defects. It occurs in combination with D', but D' is more strongly influenced by the type of defects (Eckmann et al., 2012). The reduction of edge defects can lead to a reduction of D' (Eckmann et al., 2012). It has been shown that different types of defects have a characteristic ratio of $I_D/I_{D'}$. Edge defects have a ratio of $I_D/I_{D'} \approx 3$, sp^3 defects (e.g. functionalization) have a ratio of $I_D/I_{D'} \approx 13$, and vacancies in the graphene layers have intermediate values ($I_D/I_{D'} \approx 7$) (Eckmann et al., 2012). If $I_D/I_{D'}$ increases, this indicates a shift in the defects from edge to bulk defects. In our case (Fig. 11a), the ratio $I_D/I_{D'}$ decreases with the deposition time and reaches values well below 3, which could be a consequence of disordered edges (Eckmann et al., 2012). The $I_D/I_{D'}$ values at short deposition times, where individual walls and edges were more clearly visible in CNW, were slightly above 3 for propane precursor and around 4.5 for PP + H_2 precursor, which could indicate the presence of other defects (bulk vacancies) besides edges.

3.2.2. *Capacitance of supercapacitor with CNW deposits on the electrodes*

CNW deposited on stainless-steel coin-cell battery spacer disks were used to fabricate supercapacitors, which were tested for specific capacitance. We also investigated the wetting of the CNW electrodes with TEABF4 solution, which served as the electrolyte in the fabricated supercapacitors. As shown in Supplementary information (Fig. S3), the electrolyte is completely absorbed into the CNW deposits, resulting in a contact angle of 0° for both precursors and for all deposition times.

The specific capacitance as a function of the deposition time is presented in Fig. 12a. The capacitance increases with increasing deposition time. Fig. 12(a) indicates that the PP + H_2 precursor performs even better; that is, its specific capacitance is higher than for the propane precursor. The trend of the curve for the specific capacitance versus the deposition time is similar to the variation of the thickness with the deposition time shown in Fig. 7. The steepness of the curve slowly decreases at higher deposition times. Whereas in the case of PP + H_2 precursor, the steepness is practically constant. The increase in specific capacitance with the deposition time was also observed by Cai et al. (2012). This was explained as a consequence of the increased density,

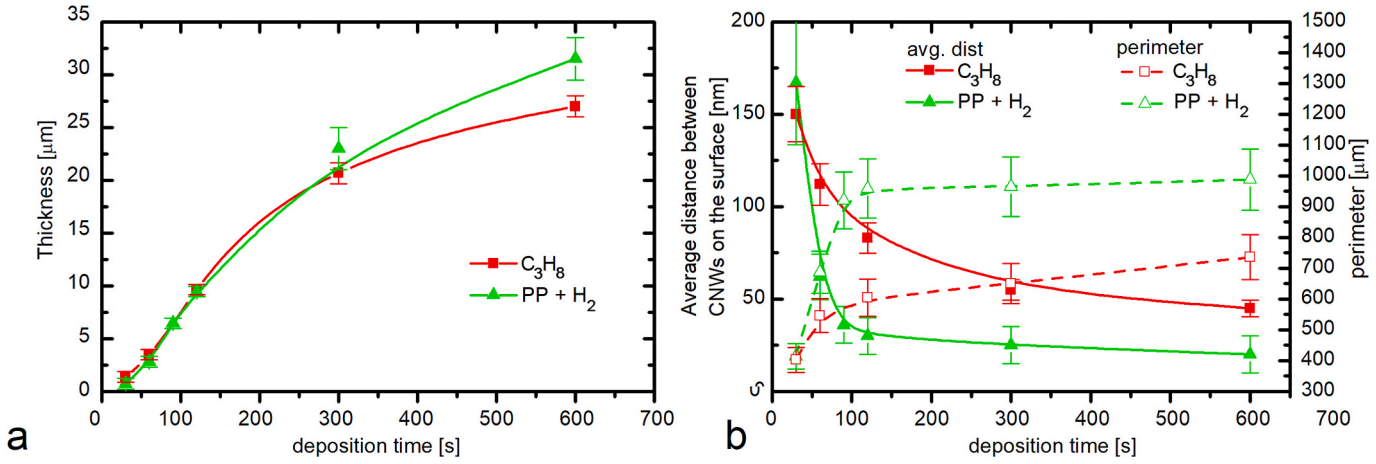

Fig. 7. The CNW thickness versus: (a) the deposition time and (b) the average distance between adjacent CNWs and perimeter of all CWNs on the surface for propane C_3H_8 and PP + H_2 precursor.

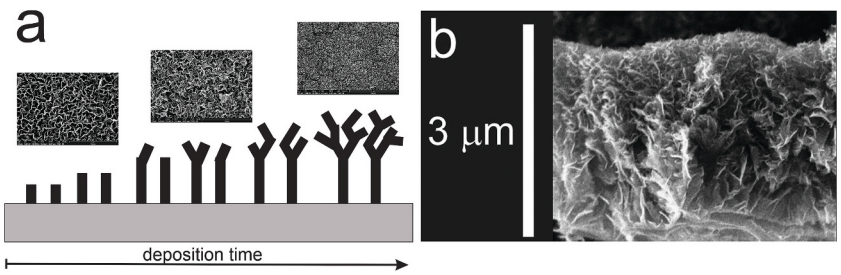

Fig. 8. Mechanism of the growth of CNW (a) and a SEM image of typical cross section of the CNW film (b).

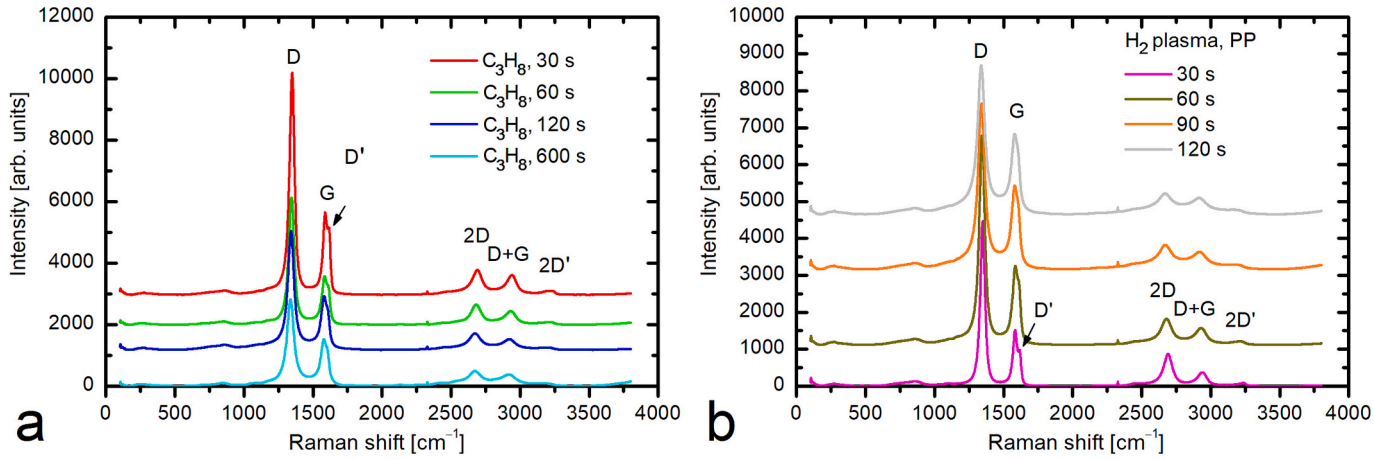

Fig. 9. Raman spectra of the CNW deposited at different deposition times in: (a) propane C_3H_8 precursor and (b) in PP + H_2 precursor.

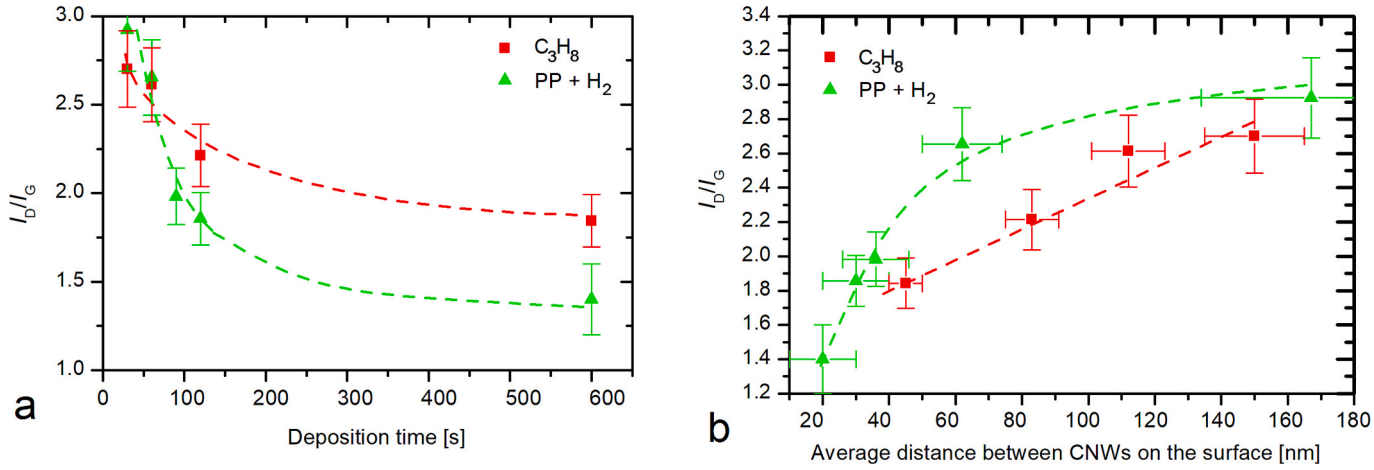

Fig. 10. The ratio of the D and G peak intensities I_D/I_G versus (a) the deposition time and (b) the average distance between CNW on the surface for propane C_3H_8 precursor and PP + H_2 precursor.

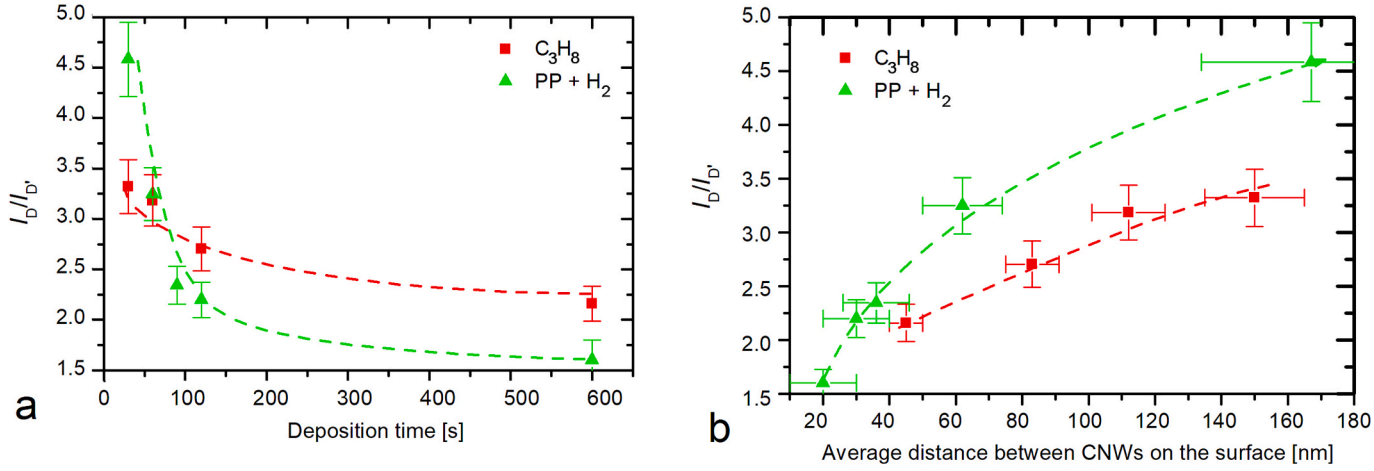

Fig. 11. The ratio of the D and D‘ peak intensities $I_D/I_{D'}$ versus: (a) the deposition time and (b) versus the average distance between CNW on the surface for propane C_3H_8 precursor and PP + H_2 precursor.

and thus the increased area/edges, of graphene-like sheets forming individual carbon nanowalls.

It can be seen that in the case of the CNW deposition performed for 120 s in the PP + H_2 precursor, its specific capacitance is more than twice of that obtained from propane, even though the thickness of the deposited CNW film is the same (Fig. 7). Therefore, the thickness of the deposits is not the only parameter that determines the specific capacitance. More important is the I_D/I_G ratio as shown in Fig. 13. In fact, the

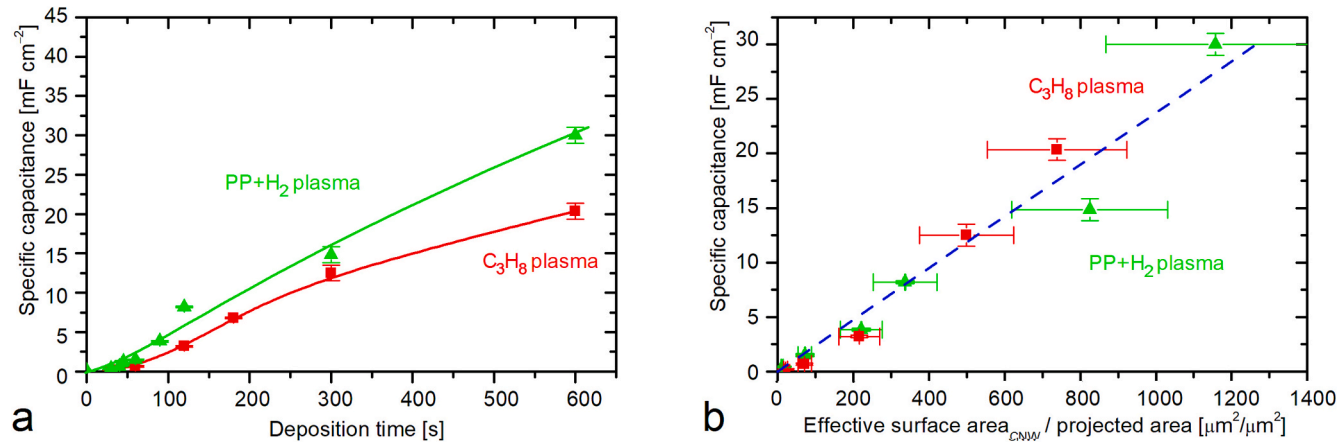

Fig. 12. The specific capacitance (C_f) at 1 Hz versus: (a) the deposition time and (b) the effective surface area of the CNW divided by the projected surface area.

specific capacitance is increasing when I_D/I_G is decreasing.

Fig. 12b shows the specific capacitance as a function of the CNW's effective surface area divided by its projected surface area. This is determined by multiplying the perimeter of the CNWs on the surface by their thickness. It should be emphasized that this is a simplified assessment and likely overestimates the ion-accessible surface area. This overestimation is particularly pronounced for the dense CNWs formed at longer deposition times. Fig. 12b clearly shows that the capacitance increases linearly with increasing effective surface area of CNWs. The linear trend in Fig. 12b suggests that, although the pore size decreases with increasing deposition time due to the higher density of the CNWs, the pore size distribution does not yet limit ion accessibility; otherwise, a decrease in capacitance would be observed (Kim et al., 2004; Chmiola et al., 2006; Heimböckel et al., 2019). This limitation, however, may arise at even longer deposition times, when the pore sizes approach the ion dimensions. The solvated ion sizes of the used electrolyte are slightly below 1 nm, while the corresponding bare ion sizes are even smaller. The surface area is important for altering the interaction between the electrode and the electrolyte, ensuring the accessibility and accumulation of ions on the electrode surface (Forse et al., 2016; Burt et al., 2016), and thus enabling the electrolyte to effectively enter small pores and access the active sites on CNWs. Therefore, Fig. 12 indicates that the mesh-like CNWs are more appropriate for supercapacitor electrodes than vertically oriented CNWs, owing to their higher active surface area, which enables greater capacitance.

The specific capacitance versus frequency is plotted in Fig. 14. The deposition time is the parameter. The specific capacitance increases with increasing deposition time, which is explained by the increasing thickness of the CNW film and, consequently, the effective surface area of the CNWs. At low frequencies, the capacitance is almost constant until it begins to decrease. For CNW electrodes with a higher specific capacitance, this occurs at lower frequencies than for those with a lower capacitance. In addition to Fig. 14, Fig. 15 shows the frequency dependence of the phase. At low frequencies, the phase angle is close to 90°, which is consistent with an ideal capacitor. The curve for PP + H_2 at 120 s of deposition time is quite flat at 90° over the frequency range up to 10 Hz (Fig. 15b), which is the optimal operating range for these electrodes. For CNW prepared in a propane precursor at 600 s of deposition time, the optimal range is much lower, up to 1 Hz. Although the specific capacitance (Fig. 14) remains stable over a much wider frequency range, the system is no longer ideally capacitive. In Fig. 16, the specific capacitance is plotted as a function of the number of cycles. It is evident that all deposited CNW remain stable up to 10,000 cycles, and the curve's stable trend suggests they will remain stable for quite a few more cycles. As reported in the literature (Wu et al., 2021), when the specific capacitance remains stable over a large number of cycles, it is likely to remain stable over many additional cycles.

Fig. 17 represents cyclic voltammetry (CV) curves measured at different scan rates for CNW electrodes formed in propane precursor with 600 s deposition time (Fig. 17a) and PP precursor with 120 s deposition time (Fig. 17b). The curves exhibit a nearly rectangular shape up to a scan rate of 2 Vs s^{-1}, which is typical for high-speed EDLC electrodes, indicating good capacitive characteristics. However, the rectangular CV of the symmetric supercapacitor of propane precursor

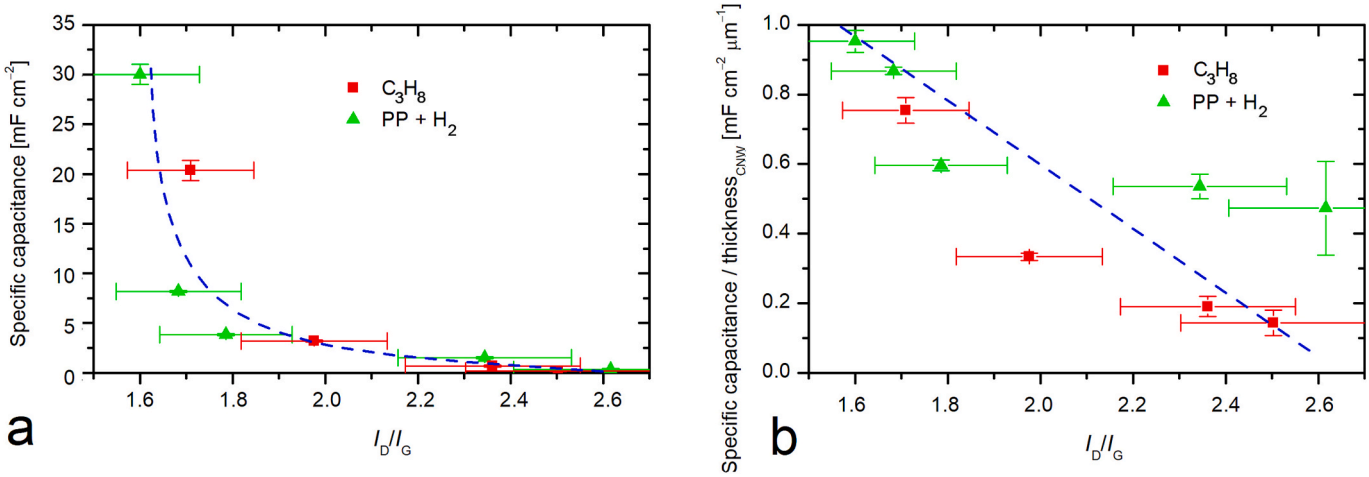

Fig. 13. (a) The specific capacitance (C_f) variation and (b) specific capacitance (C_f) divided by the thickness of the CNWs versus the I_D/I_G ratio.

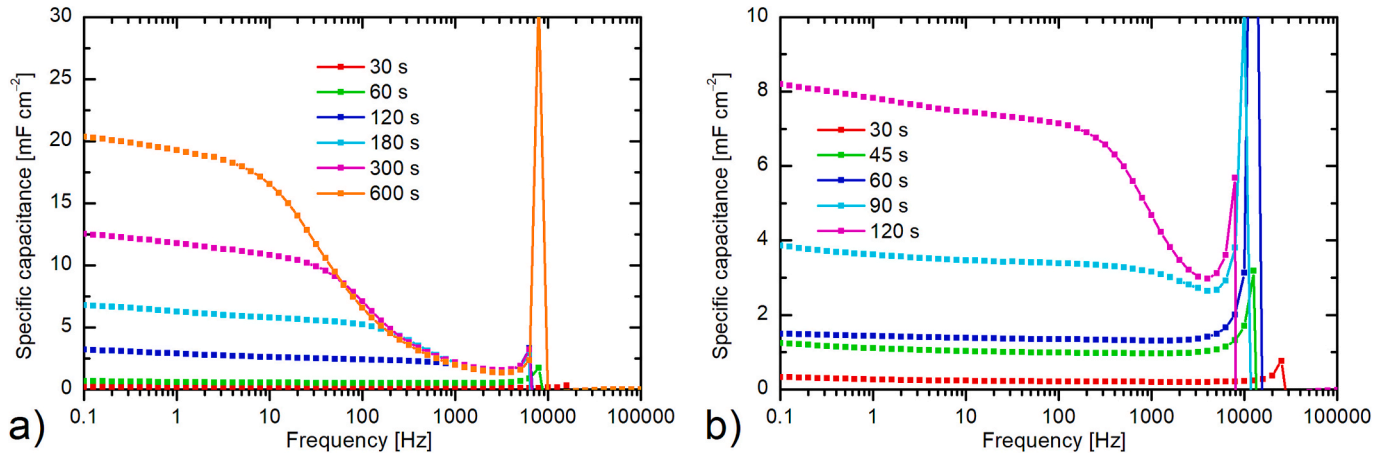

Fig. 14. Specific capacitance (C_f) of the capacitors versus the frequency for: (a) propane precursor and (b) PP + H_2 precursor.

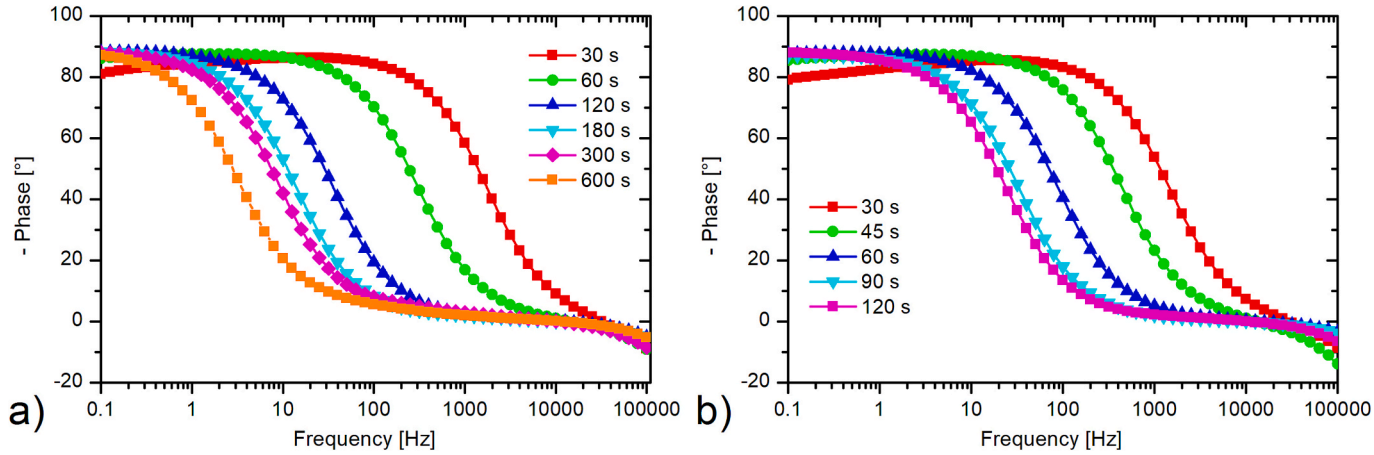

Fig. 15. Phase of the capacitors versus the frequency for: (a) propane precursor and (b) PP + H_2 precursor.

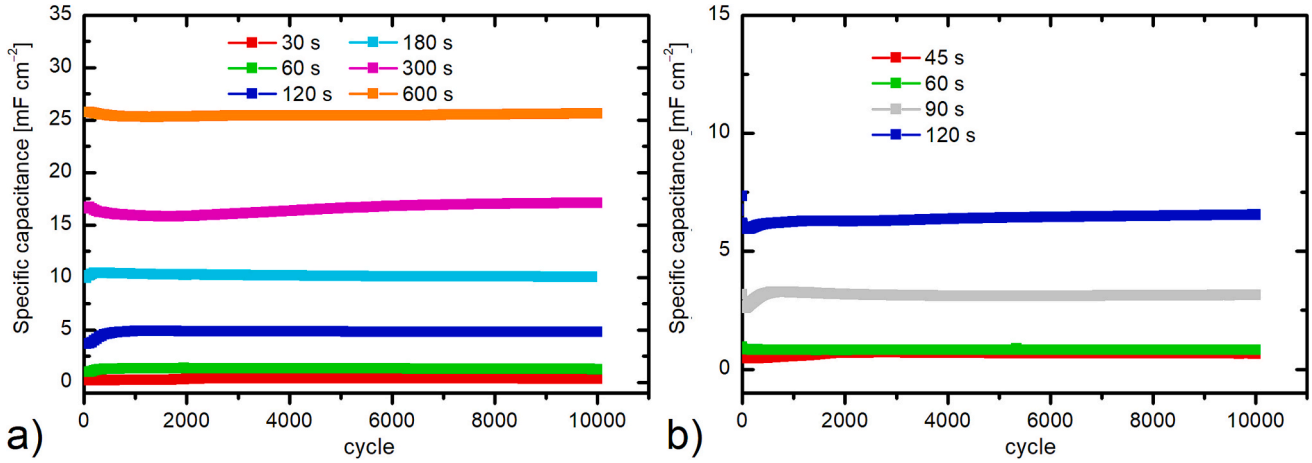

Fig. 16. Specific capacitance of the capacitors versus the number of the cycles for: (a) propane precursor and (b) PP + H_2 precursor.

with 600 s deposition tends to be spindle-shaped when the scan rate continues to increase, whereas that of the supercapacitor of PP + H_2 precursor with 120 s deposition is still rectangular in shape. It indicates that the dense all-directional growth of CNW due to the long-time deposition increases the tortuosity, hindering the ionic transport, as discussed before in connection with morphology. The electrode of PP + H_2 precursor with a deposition time of 120 s still maintains vertically open pores for the ions transport directly from the surface to the bottom of the electrode. Fig. 18 shows the GCD curves measured at different current densities. The curves show a linear rise and fall of the voltage during the charging and discharging of the samples, indicating the ideal capacitive behavior of EDLC. The curves are fairly symmetrical, confirming the high stability of the electrodes and reversible charge storage.

Finally, we can compare our results of specific capacitance with

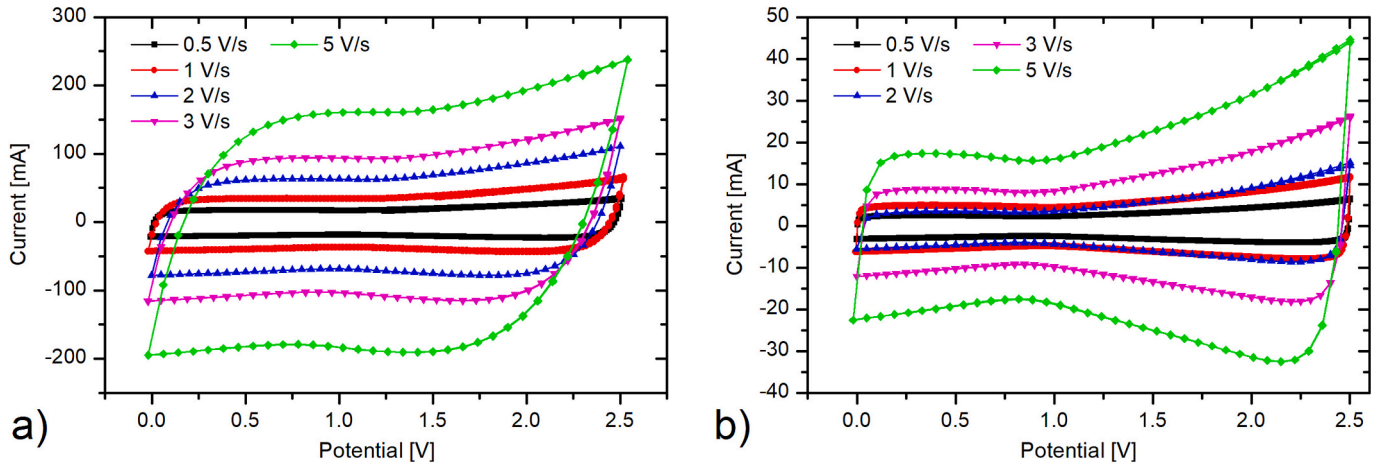

Fig. 17. Cyclic voltammogram for: (a) propane precursor with a deposition time of 600 s and (b) PP precursor with a deposition time of 120 s.

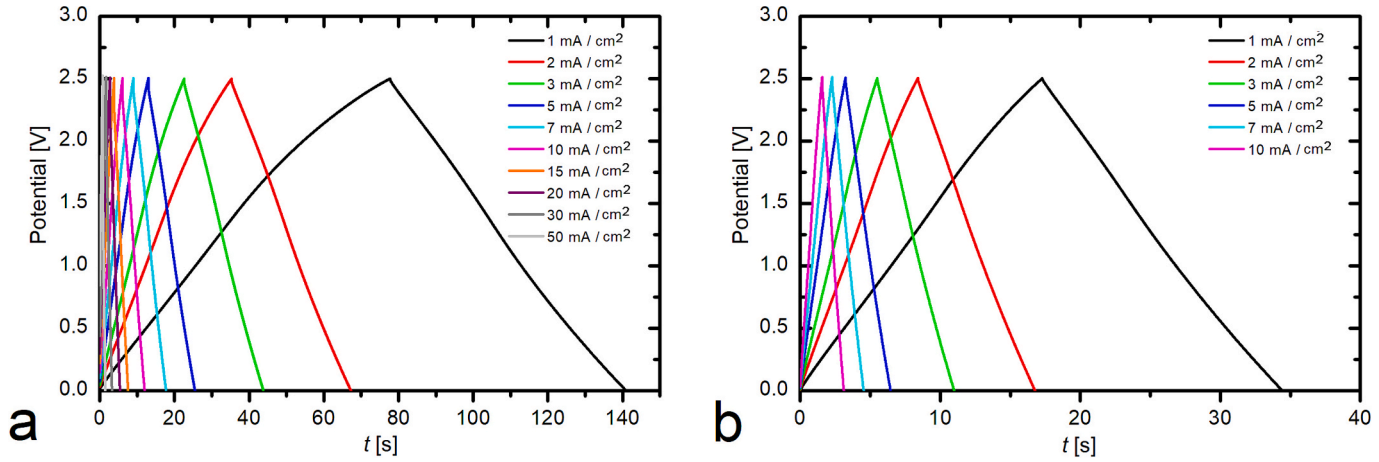

Fig. 18. Charging-discharging curves for (a) propane precursor with a deposition time of 600 s and (b) PP precursor with a deposition time of 120 s.

those in the literature. Table 1 compares the reported capacitance obtained for CNW electrodes. From this comparison, we can conclude that we achieved very high specific capacities, i.e., 25 mF cm^{-2}, compared to other authors, which indicates the high potential of our electrodes made of CNWs.

The experiments reported in this article were performed in a small plasma reactor. The inner diameter of the discharge tube was 3.6 mm, and the length of the dense plasma with a high luminosity was roughly 10 cm. Any application of the method disclosed in this article would require larger plasma reactors, and deposition should preferably be performed in a continuous mode, i.e., moving the substrate through a dense plasma while continuously feeding waste plastics into the dense plasma zone. The plasma parameters should be similar to those achievable in the experimental reactor, which is illustrated in Fig. 1. Such an upscaling is scientifically feasible but represents a technological challenge. It is well known that a dense inductively coupled RF plasma in the H mode is confined in a rather small volume due to the requirement for a critical plasma conductivity. Details about the limitations for upscaling RF ICP in the H mode are explained in (Zaplotnik et al., 2021). Briefly, sustaining of plasma in the H mode at a reasonable power density (discharge power absorbed in a plasma volume) is feasible only in rather narrow tubes. The plasma length in H mode is limited by the coil impedance, which increases with increasing coil length. This limitation may be overcome by using several ICP sources mounted in series, thereby increasing the plasma length. The power required to sustain plasma may be an obstacle, but using waste materials to synthesize useful products may compensate for the rather high-power density needed to sustain plasma, which is useful for depositing nanocarbon electrodes.

The waste plastic used as carbon precursor was waste polypropylene. Other types of waste plastics (preferably with a low concentration of other elements but carbon and hydrogen) could also be used. According to our recent publication (Vesel et al., 2022), different polymers can be used for CNW deposition, but the morphology and deposition rates vary slightly with the type of polymer.

The cost of depositing methods will depend on the peculiarities of the system, but the major cost arises from the electricity spent on pumping the plasma reactor and sustaining the discharge. In our particular case, we used a vacuum pump with a nominal power of 2400 W. However, the real power required by the pump at low pressure is much lower. We connected a power meter and measured power during continuous pumping at 16 Pa. It was about 1400 W. We also installed the power meter in series with the RF generator, and it measured about 540 W at a forward power of 500 W. Therefore, the total power was about 1940 W.

Fig. 12(a) shows that the capacitance of our prototype supercapacitors gained in a unit deposition time is roughly 0.05 mF cm^{-2} s^{-1}. Considering the power required for electricity, the gain (reverse of the energy cost of our prototypes) is approximately 0.1F cm^{-2} kWh^{-1}. If the cost of electricity is 0.2 € / kWh, the cost of our prototype is about 2 € for a capacitor with a capacitance of 1F/cm^2. This is much larger than the cost of commercial graphene supercapacitors, but we should stress that we calculated this value for our particular experimental system, where

Table 1
Review of specific capacitance of vertically-oriented graphene-like sheets as reported by various authors.

Material	I_D/I_G	Electrolyte	Capacitance	Current density	Scan rate or frequency	Ref.
CNW (from PP + H_2)	1.5	$TEABF_4$/ACN	30 mF/cm^2	6 mA/cm^2		this study
CNW (from propane)	1.8	$TEABF_4$/ACN	20 mF/cm^2	4 /cm^2		this study
CNW	/	6 M KOH	1.32 mF/cm^2 0.32 mF/cm^2		1 V/s 1 kHz	(Ren et al., 2014)
CNW	1.1	0.1 M Na_2SO_4	230F/g	10 mV/s		(Seo et al., 2013)
CNW	0.7	1 M Na_2SO_4	0.46F/cm^2 156F/g	5 mV/s		(Seo et al., 2015)
CNW	0.5	25 wt% KOH	0.12 mF/cm^2		1 kHz	(Cai et al., 2012)
CNW/CNT	0.51	0.5 M H_2SO_4	176F/g	0.5 mA/cm^2		(Hsu et al., 2012)
CNW	/	H_2SO_4 $TEABF_4/H_2SO_4$ $TEABF_4/H_2SO_4$ + activated with KOH	0.64 mF/cm^2 1.99 mF/cm^2 3.31 mF/cm^2			(Ghosh et al., 2017)
CNW	1.4	1 M KOH	0.156 mF/cm^2 as grown 1.646 mF/cm^2 after O_2 plasma treatment			(Sahoo et al., 2018)
CNW	/	1 M NaAc /1M $MgSO_4$	0.962 mF/cm^2 after O_2 plasma treatment	0.035 mA/cm^2		(Zhou et al., 2016)
CNW	/	1 M H_2SO_4	105F/g as grown 600F/g after N_2 plasma treatment		20 mV/s	(Evlashin et al., 2019)
CNW	/	1 M Na_2SO_4	0.922 and 0.167 mF/cm^2 for wettability of 16° and 141°, respectively			(Deheryan et al., 2014)
CNW	/		312F/g 148F/g		10 mV/s 500 mV/s	(Kumar et al., 2019)
ZnO/CNW		1 M KCl	4.3 mF/cm^2 1.41 mF/cm^2	0.2 mA/cm^2	 10 mV/s	(Guerra et al., 2019)
MgO_2/CNW		1 M Na_2SO_4	104F/g		150 mV/s	(Amade et al., 2019)
MnO_2/CNW		0.5 M Na_2SO_4	851F/g	1 mA/cm^2		(Hassan et al., 2014)
MnO_2/CNW/CNT		1 M Na_2SO_4	230 mF/cm^2 560F/g		10 mV/s	(Amade et al., 2021)
MoS_2/CNW		DMF (dimethylformamide) ACN (acetonitrile)	33 mF/cm^2 20 mF/cm^2		10 mV/s	(Shin et al., 2022)
RuO_2/CNW		2 M KOH	1000 mF/cm^2	1.5 mA/cm^2		(Dinh et al., 2014)
WO_x/CNW		0.5 M H_2SO_4	1247.2 mF/cm^2	1 mA/cm^2		(Coman et al., 2023)
NiCo-MOF/CNW		2 M KOH	950F/g	1 A/g		(Sahoo et al., 2023)
Ni-MOF/CNW		0.1 M $Ni(NO_3)_2$	677F/g	2 A/g		(Zhang et al., 2021)
B-doped CNW		1 M Na_2SO_4	0.43 mF/cm^2			(Banerjee et al., 2019)

small substrates were placed in the dense plasma. Fig. 1 and the accompanying text suggest that the size of the substrates for our system could be an order of magnitude larger. Optimization in terms of upscaling the reactor would probably add another order of magnitude (if not more so), so the likely energy cost of production supercapacitors according to the method disclosed in this article is close to 0.02 € for a capacitor with the capacitance of 1F/cm^2.

4. Conclusions

Two different precursors were used for the growth of carbon nanowalls composed of vertically oriented multilayer graphene-like sheets on the surface of electrodes for supercapacitors. By increasing the deposition time, a multi-layered structure of interconnected and dense graphene-like walls was obtained for both precursors. For the PP + H_2 precursor, a dense interconnected structure was formed at shorter deposition times than for the propane precursor. Nevertheless, both precursors lead to a similar deposition rate. The deposited interconnected structure represented a mesh with a large specific surface area that had a beneficial effect on the electrical characteristics of supercapacitors and their capacitance. The I_D/I_G ratio decreases with the deposition time for both precursors, and the specific capacitance monotonously increases with the deposition time. Specific capacitance increases as I_D/I_G ratio decreases. It was found that the specific capacitance was linearly proportional to the effective surface area, which was increasing with increasing deposition time. The specific capacitance versus the deposition time was increasing faster for the PP + H_2 precursor, for which also the highest capacitance was obtained. The maximum specific capacitance obtained for PP + H_2 and propane precursors was 30 and 25 mF/cm^{-2}, respectively. The cyclic voltammetry curves were typical for EDLC capacitors. The results presented in this article show that plastic is a suitable precursor for the deposition of carbon nanomaterials for application in electrochemical devices, thus offering the possibility to replace fossil hydrocarbons with waste plastics. Our study demonstrates a concept for converting plastic materials into new functional materials for energy applications, thereby contributing to circular material utilization.

CRediT authorship contribution statement

Alenka Vesel: Writing – original draft, Validation, Resources, Project administration, Methodology, Funding acquisition, Conceptualization. **Gregor Primc:** Investigation, Formal analysis, Data curation. **Miran Mozetič:** Writing – review & editing, Supervision, Resources, Funding acquisition. **Melita Tramšek:** Writing – review & editing, Investigation, Formal analysis. **Evelin Gruden:** Investigation, Formal

analysis. **Haojie Fei:** Writing – review & editing, Visualization, Investigation, Formal analysis, Data curation. **Peter Saha:** Validation, Supervision. **Marian Lehocky:** Supervision, Funding acquisition. **Rok Zaplotnik:** Writing – original draft, Visualization, Investigation, Formal analysis, Data curation, Conceptualization.

Declaration of competing interest

The authors declare that they have no known competing financial interests or personal relationships that could have appeared to influence the work reported in this paper.

Acknowledgements

This research was funded by the Slovenian Research Agency, project L2-50052 “Supercapacitors with graphene nanowalls synthesized from waste plastics””, project L2-60139 “Innovative plasma-assisted synthesis of the next-generation high power density supercapacitor electrodes using graphene oxide feedstock ”, and core funding P2-0082 “Thin-film structures and plasma surface engineering”. The research was also supported by the Ministry of Education, Youth and Sports of the Czech Republic–DKRVO (RP/CPS/2024-28/005).

Appendix A. Supplementary data

The supplementary material provides additional information on the mass of the deposited CNWs, their chemical composition measured by XPS, and their wettability with electrolyte. Supplementary data to this article can be found online at https://doi.org/10.1016/j.clema.2026.100397.

Data availability

The data supporting the findings of this study are available in Zenodo at DOI: 10.5281/zenodo.15863573.

References

Amade, R., Muyshegyan-Avetisyan, A., Martí González, J., Pérez Del Pino, A., György, E., Pascual, E., Andújar, J.L., Bertran Serra, E., 2019. Super-capacitive performance of manganese dioxide/graphene nano-walls electrodes deposited on stainless steel current collectors. Materials 12, 483. https://doi.org/10.3390/ma12030483.

Amade, R., Alshaikh, I., Musheghyan-Avetisyan, A., Bertran-Serra, E., 2021. Enhanced capacitance of manganese oxide driven by hierarchically structured carbon nanotube-carbon nanowall composite. Surf. Coat. Technol. 428, 127885. https://doi.org/10.1016/j.surfcoat.2021.127885.

Banerjee, D., Sankaran, K.J., Deshmukh, S., Ficek, M., Bhattacharya, G., Ryl, J., Phase, D. M., Gupta, M., Bogdanowicz, R., Lin, I.N., Kanjilal, A., Haenen, K., Roy, S.S., 2019. 3D Hierarchical boron-doped diamond-multilayered graphene nanowalls as an efficient supercapacitor electrode. J. Phys. Chem. C 123, 15458–15466. https://doi.org/10.1021/acs.jpcc.9b03628.

Burt, R., Breitsprecher, K., Daffos, B., Taberna, P.-L., Simon, P., Birkett, G., Zhao, X.S., Holm, C., Salanne, M., 2016. Capacitance of nanoporous carbon-based supercapacitors is a trade-off between the concentration and the separability of the Ions. J. Phys. Chem. Lett. 7, 4015–4021. https://doi.org/10.1021/acs.jpclett.6b01787.

Cai, M., Outlaw, R.A., Butler, S.M., Miller, J.R., 2012. A high density of vertically-oriented graphenes for use in electric double layer capacitors. Carbon 50, 5481–5488. https://doi.org/10.1016/j.carbon.2012.07.035.

Chmiola, J., Yushin, G., Gogotsi, Y., Portet, C., Simon, P., Taberna, P.L., 2006. Anomalous increase in carbon capacitance at pore sizes less than 1 nanometer. Science 313, 1760–1763. https://doi.org/10.1126/science.1132195.

Coman, L.G., Marcu, M., Acsente, T., Vizireanu, S., Satulu, V., Dinescu, G., Matei, E., Spataru, T., Spataru, N., Preda, L., 2023. Hybrid nanostructures based on vertically graphenes decorated with tungsten oxide nanoparticles for enhanced capacitive performance. Diam. Relat. Mater. 139, 110316. https://doi.org/10.1016/j.diamond.2023.110316.

Cui, L., Chen, J., Yang, B., Sun, D., Jiao, T., 2015. RF-PECVD synthesis of carbon nanowalls and their field emission properties. Appl. Surf. Sci. 357, 1–7. https://doi.org/10.1016/j.apsusc.2015.08.252.

Davami, K., Shaygan, M., Kheirabi, N., Zhao, J., Kovalenko, D.A., Rümmeli, M.H., Opitz, J., Cuniberti, G., Lee, J.-S., Meyyappan, M., 2014. Synthesis and characterization of carbon nanowalls on different substrates by radio frequency plasma enhanced chemical vapor deposition. Carbon 72, 372–380. https://doi.org/10.1016/j.carbon.2014.02.025.

Deheryan, S.J., Cott, D.W., Mertens, P., Heyns, M.M., Vereecken, P., 2014. Direct correlation between the measured electrochemical capacitance, wettability and surface functional groups of CarbonNanosheets. Electrochim. Acta 132, 574–582. https://doi.org/10.1016/j.electacta.2014.03.148.

Denysenko, I.B., Von Wahl, E., Mikikian, M., Berndt, J., Ivko, S., Kersten, H., Kovacevic, E., Azarenkov, N.A., 2020. Plasma properties as function of time in Ar/C_2H_2 dust-forming plasma. J. Phys. D Appl. Phys. 53, 135203. https://doi.org/10.1088/1361-6463/ab6625.

Dinh, T.M., Achour, A., Vizireanu, S., Dinescu, G., Nistor, L., Armstrong, K., Guay, D., Pech, D., 2014. Hydrous RuO_2/carbon nanowalls hierarchical structures for all-solid-state ultrahigh-energy-density micro-supercapacitors. Nano Energy 10, 288–294. https://doi.org/10.1016/j.nanoen.2014.10.003.

Eckmann, A., Felten, A., Mishchenko, A., Britnell, L., Krupke, R., Novoselov, K.S., Casiraghi, C., 2012. Probing the nature of defects in graphene by Raman spectroscopy. Nano Lett. 12, 3925–3930. https://doi.org/10.1021/nl300901a.

Evlashin, S.A., Maksimov, Y.M., Dyakonov, P.V., Pilevsky, A.A., Maslakov, K.I., Mankelevich, Y.A., Voronina, E.N., Vavilov, S.V., Pavlov, A.A., Zenova, E.V., Akhatov, I.S., Suetin, N.V., 2019. N-doped carbon nanowalls for power sources. Sci. Rep. 9, 6716. https://doi.org/10.1038/s41598-019-43001-3.

Forse, A.C., Merlet, C., Griffin, J.M., Grey, C.P., 2016. New perspectives on the charging mechanisms of supercapacitors. J. Am. Chem. Soc. 138, 5731–5744. https://doi.org/10.1021/jacs.6b02115.

Gentoiu, M.A., Betancourt-Riera, R., Vizireanu, S., Burducea, I., Marascu, V., Stoica, S.D., Bita, B.I., Dinescu, G., Riera, R., 2017. Morphology, microstructure, and hydrogen content of carbon nanostructures obtained by PECVD at various temperatures. J. Nanomater. 2017, 1374973. https://doi.org/10.1155/2017/1374973.

Ghosh, S., Sahoo, G., Polaki, S.R., Krishna, N.G., Kamruddin, M., Mathews, T., 2017. Enhanced supercapacitance of activated vertical graphene nanosheets in hybrid electrolyte. J. Appl. Phys. 122, 214902. https://doi.org/10.1063/1.5002748.

Guerra, A., Achour, A., Vizireanu, S., Dinescu, G., Messaci, S., Hadjersi, T., Boukherroub, R., Coffinier, Y., Pireaux, J.-J., 2019. ZnO/Carbon nanowalls shell/core nanostructures as electrodes for supercapacitors. Appl. Surf. Sci. 481, 926–932. https://doi.org/10.1016/j.apsusc.2019.03.204.

Haomin, W, Yihong, W, Choong, CKS, Jun, Z, Kie Leong, T, Zhenhua, N, Zexiang, S. Disorder induced bands in first order Raman spectra of carbon nanowalls. 2006 Sixth IEEE Conf on Nanotechnology, 17–20 July 2006 2006. 219-222.

Hassan, S., Suzuki, M., Mori, S., El-Moneim, A.A., 2014. MnO_2/carbon nanowalls composite electrode for supercapacitor application. J. Power Sources 249, 21–27. https://doi.org/10.1016/j.jpowsour.2013.10.097.

Heimböckel, R., Hoffmann, F., Fröba, M., 2019. Insights into the influence of the pore size and surface area of activated carbons on the energy storage of electric double layer capacitors with a new potentially universally applicable capacitor model. PCCP 21, 3122–3133. https://doi.org/10.1039/C8CP06443A.

Hiramatsu, M, Kondo, H, Hori, M, 2013. Graphene Nanowalls. In: New Progress on Graphene Research. Ed. Gong, J.R. IntechOpen. https://doi.org/10.5772/51528.

Hori, M, Hiramatsu, M, Kano, H, 2011. Method for producing carbon nanowalls. US2011045207A1.

Hsu, H.-C., Wang, C.-H., Nataraj, S.K., Huang, H.-C., Du, H.-Y., Chang, S.-T., Chen, L.-C., Chen, K.-H., 2012. Stand-up structure of graphene-like carbon nanowalls on CNT directly grown on polyacrylonitrile-based carbon fiber paper as supercapacitor. Diam. Relat. Mater. 25, 176–179. https://doi.org/10.1016/j.diamond.2012.02.020.

Itoh, T., Shimabukuro, S., Kawamura, S., Nonomura, S., 2006. Preparation and electron field emission of carbon nanowall by Cat-CVD. Thin Solid Films 501, 314–317. https://doi.org/10.1016/j.tsf.2005.07.216.

Kim, Y.J., Horie, Y., Ozaki, S., Matsuzawa, Y., Suezaki, H., Kim, C., Miyashita, N., Endo, M., 2004. Correlation between the pore and solvated ion size on capacitance uptake of PVDC-based carbons. Carbon 42, 1491–1500. https://doi.org/10.1016/j.carbon.2004.01.049.

Kim, S.Y., Shin, S.K., Kim, H., Jung, Y.-H., Kang, H.-I., Choi, W.S., Kweon, G.B., 2015. Synthesis of carbon nanowalls by microwave PECVD for battery electrode. Trans. Electr. Electron. Mater. 16, 198–200. https://doi.org/10.4313/TEEM.2015.16.4.198.

Kondo, S., Kawai, S., Takeuchi, W., Yamakawa, K., Den, S., Kano, H., Hiramatsu, M., Hori, M., 2009. Initial growth process of carbon nanowalls synthesized by radical injection plasma-enhanced chemical vapor deposition. J. Appl. Phys. 106, 094302. https://doi.org/10.1063/1.3253734.

Kumar, S., Martin, P., Bendavid, A., Bell, J., Ostrikov, K., 2019. Oriented graphenes from plasma-reformed coconut oil for supercapacitor electrodes. Nanomaterials 9, 1679. https://doi.org/10.3390/nano9121679.

Largeot, C., Portet, C., Chmiola, J., Taberna, P.-L., Gogotsi, Y., Simon, P., 2008. Relation between the ion size and pore size for an electric double-layer capacitor. J. Am. Chem. Soc. 130, 2730–2731. https://doi.org/10.1021/ja7106178.

Lehmann, K., Yurchenko, O., Urban, G., 2016. Effect of the aromatic precursor flow rate on the morphology and properties of carbon nanostructures in plasma enhanced chemical vapor deposition. RSC Adv. 6, 32779–32788. https://doi.org/10.1039/C6RA02999J.

Maduraiveeran, G., Jin, W., 2021. Carbon nanomaterials: Synthesis, properties and applications in electrochemical sensors and energy conversion systems. Mat Sci Eng B 272, 115341. https://doi.org/10.1016/j.mseb.2021.115341.

Manawi, Y.M., Ihsanullah, S.A., Al-Ansari, T., Atieh, M.A., 2018. A review of carbon nanomaterials' synthesis via the chemical vapor deposition (CVD) method. Materials 11, 822. https://doi.org/10.3390/ma11050822.

Meško, M., Vretenár, V., Kotrusz, P., Hulman, M., Šoltýs, J., Skákalová, V., 2012. Carbon nanowalls synthesis by means of atmospheric dcPECVD method. Phys. Status Solidi B 249, 2625–2628. https://doi.org/10.1002/pssb.201200144.

Ni, Z.H., Fan, H.M., Feng, Y.P., Shen, Z.X., Yang, B.J., Wu, Y.H., 2006. Raman spectroscopic investigation of carbon nanowalls. J. Chem. Phys. 124, 204703. https://doi.org/10.1063/1.2200353.

Paul, D., Zaplotnik, R., Primc, G., Vesel, A., Mozetič, M., 2024. Evolution of the surface wettability of vertically oriented multilayer graphene sheets deposited by plasma technology. Nanomaterials 14, 1023. https://doi.org/10.3390/nano14121023.

Ren, G., Pan, X., Bayne, S., Fan, Z., 2014. Kilohertz ultrafast electrochemical supercapacitors based on perpendicularly-oriented graphene grown inside of nickel foam. Carbon 71, 94–101. https://doi.org/10.1016/j.carbon.2014.01.017.

Sahoo, G., Polaki, S.R., Ghosh, S., Krishna, N.G., Kamruddin, M., 2018. Temporal-stability of plasma functionalized vertical graphene electrodes for charge storage. J. Power Sources 401, 37–48. https://doi.org/10.1016/j.jpowsour.2018.08.071.

Sahoo, G., Jeong, H.S., Polaki, S.R., Jeong, S.M., 2023. Vertical graphene nanosheets as interface current-collector for enhanced charge-storage kinetics of bimetallic MOF nano-rods and asymmetric solid-state supercapacitors. J Energy Storage 68, 107824. https://doi.org/10.1016/j.est.2023.107824.

Sahoo, S., Sahoo, G., Jeong, S.M., Rout, C.S., 2022. A review on supercapacitors based on plasma enhanced chemical vapor deposited vertical graphene arrays. J Energy Storage 53, 105212. https://doi.org/10.1016/j.est.2022.105212.

Schuepfer, D.B., Badaczewski, F., Guerra-Castro, J.M., Hofmann, D.M., Heiliger, C., Smarsly, B., Klar, P.J., 2020. Assessing the structural properties of graphitic and non-graphitic carbons by Raman spectroscopy. Carbon 161, 359–372. https://doi.org/10.1016/j.carbon.2019.12.094.

Seo, D.H., Han, Z.J., Kumar, S., Ostrikov, K., 2013. Structure-controlled, vertical graphene-based, binder-free electrodes from plasma-reformed butter enhance supercapacitor performance. Adv Energ Mat 3, 1316–1323. https://doi.org/10.1002/aenm.201300431.

Seo, D.H., Yick, S., Pineda, S., Su, D., Wang, G., Han, Z.J., Ostrikov, K., 2015. Single-step, plasma-enabled reforming of natural precursors into vertical graphene electrodes with high areal capacitance. ACS Sustain Chem Eng Acta 3, 544–551. https://doi.org/10.1021/sc500806s.

Shiji, K., Hiramatsu, M., Enomoto, A., Nakamura, N., Amano, H., Hori, M., 2005. Vertical growth of carbon nanowalls using rf plasma-enhanced chemical vapor deposition. Diam. Relat. Mater. 14, 831–834. https://doi.org/10.1016/j.diamond.2004.10.021.

Shimabukuro, S., Hatakeyama, Y., Takeuchi, M., Itoh, T., Nonomura, S., 2008. Effect of hydrogen dilution in preparation of carbon nanowall by hot-wire CVD. Thin Solid Films 516, 710–713. https://doi.org/10.1016/j.tsf.2007.06.181.

Shin, J.-H., Choi, Y.-S., Park, H.-J., 2022. Remote plasma-induced synthesis of self-assembled MoS_2/carbon nanowall nanocomposites and their application as high-performance active materials for supercapacitors. Nanomaterials 12, 1338. https://doi.org/10.3390/nano12081338.

Teii, K., Shimada, S., Nakashima, M., Chuang, A.T.H., 2009. Synthesis and electrical characterization of n-type carbon nanowalls. J. Appl. Phys. 106, 084303 https://doi.org/8430310.1063/1.3238276.

Vesel, A., Zaplotnik, R., Primc, G., Mozetič, M., 2019. Synthesis of vertically oriented graphene sheets or carbon nanowalls—review and challenges. Materials 12, 2968. https://doi.org/10.3390/ma12182968.

Vesel, A., Zaplotnik, R., Primc, G., Mozetič, M., 2020. A review of strategies for the synthesis of N-doped graphene-like materials. Nanomaterials 10, 2286. https://doi.org/10.3390/nano10112286.

Vesel, A., Zaplotnik, R., Primc, G., Pirker, L., Mozetič, M., 2021. One-step plasma synthesis of nitrogen-doped carbon nanomesh. Nanomaterials 11, 837. https://doi.org/10.3390/nano11040837.

Vesel, A., Zaplotnik, R., Primc, G., Paul, D., Mozetič, M., 2022. Comparison of plasma deposition of carbon nanomaterials using various polymer materials as a carbon atom source. Nanomaterials 12, 246. https://doi.org/10.3390/nano12020246.

Vizireanu, S., Mitu, B., Luculescu, C.R., Nistor, L.C., Dinescu, G., 2012. PECVD synthesis of 2D nanostructured carbon material. Surf. Coat. Technol. 211, 2–8. https://doi.org/10.1016/j.surfcoat.2011.07.092.

Wu, J., 2022. Understanding the electric double-layer structure, capacitance, and charging dynamics. Chem. Rev. 122, 10821–10859. https://doi.org/10.1021/acs.chemrev.2c00097.

Wu, Q., He, T., Zhang, Y., Zhang, J., Wang, Z., Liu, Y., Zhao, L., Wu, Y., Ran, F., 2021. Cyclic stability of supercapacitors: materials, energy storage mechanism, test methods, and device. J. Mater. Chem. A 9, 24094–24147. https://doi.org/10.1039/D1TA06815F.

Wu, Z., Wang, E., Zhang, G., Shen, Y., Shao, G., 2024. Recent progress of vertical graphene: preparation, structure engineering, and emerging energy applications. Small 20, 2307923. https://doi.org/10.1002/smll.202307923.

Yen, H.F., Horng, Y.Y., Hu, M.S., Yang, W.H., Wen, J.R., Ganguly, A., Tai, Y., Chen, K.H., Chen, L.C., 2015. Vertically aligned epitaxial graphene nanowalls with dominated nitrogen doping for superior supercapacitors. Carbon 82, 124–134. https://doi.org/10.1016/j.carbon.2014.10.042.

Yerlanuly, Y., Zhumadilov, R., Nemkayeva, R., Uzakbaiuly, B., Beisenbayev, A.R., Bakenov, Z., Ramazanov, T., Gabdullin, M., Ng, A., Brus, V.V., Jumabekov, A.N., 2021. Physical properties of carbon nanowalls synthesized by the ICP-PECVD method vs. the growth time. Sci. Rep. 11, 19287. https://doi.org/10.1038/s41598-021-97997-8.

Yoon, D., Cheong, H., 2012. In: Raman Spectroscopy for Characterization of Graphene. in: Raman Spectroscopy for Characterization. Springer, Berlin, Heidelberg. https://doi.org/10.1007/978-3-642-20620-7_9.

Zaplotnik, R, Primc, G, Paul, D, Mozetič, M, Kovač, J, Vesel, A, 2021. Atomic Species Generation by Plasmas. In: Plasma Applications for Material Modification: From Microelectronics to Biological Materials. Ed. Tabarés, F.L. Jenny Stanford Publishing. https://doi.org/10.1201/9781003119203.

Zeng, J.J., Lin, Y.J., 2014. Tuning the work function of graphene by nitrogen plasma treatment with different radio-frequency powers. Appl. Phys. Lett. 104, 233103. https://doi.org/10.1063/1.4882159.

Zhang, J., Wang, Z., Deng, T., Zhang, W., 2021. $Ni(OH)_2$ derived Ni-MOF supported on carbon nanowalls for supercapacitors. Nanotechnology 32, 195404. https://doi.org/10.1088/1361-6528/abdf8e.

Zhang, H., Wu, S., Lu, Z., Chen, X., Chen, Q., Gao, P., Yu, T., Peng, Z., Ye, J., 2019. Efficient and controllable growth of vertically oriented graphene nanosheets by mesoplasma chemical vapor deposition. Carbon 147, 341–347. https://doi.org/10.1016/j.carbon.2019.01.042.

Zhao, Z., Zhang, W., Wang, D., Li, L., Liang, Q., Li, W., Lu, C., Jo Yoo, S., Kim, J.-G., Chen, Z., Li, Y., Zou, X., Liu, F., Zhou, X., Song, K., Li, J., Zheng, W., 2024. Ostwald-ripening induced interfacial protection layer boosts 1,000,000-cycled hydronium-ion battery. Angew. Chem. Int. Ed. 63, e202414420. https://doi.org/10.1002/anie.202414420.

Zhou, H.T., Liu, D.B., Luo, F., Luo, B.W., Tian, Y., Chen, D.S., Shen, C.M., 2018. Preparation of graphene nanowalls on nickel foam as supercapacitor electrodes. Micro Nano Lett. 13, 842–844. https://doi.org/10.1049/mnl.2017.0922.

Zhou, H.-T., Yu, N., Zou, F., Yao, Z.-H., Gao, G., Shen, C.-M., 2016. Controllable preparation of vertically standing graphene sheets and their wettability and supercapacitive properties. Chin. Phys. B 25, 096106. https://doi.org/10.1088/1674-1056/25/9/096106.

Zólyomi, V., Koltai, J., Kürti, J., 2011. Resonance Raman spectroscopy of graphite and graphene. Phys. Status Solidi B 248, 2435–2444. https://doi.org/10.1002/pssb.201100295.

Zuliani, J.E., Tong, S., Jia, C.Q., Kirk, D.W., 2018. Contribution of surface oxygen groups to the measured capacitance of porous carbon supercapacitors. J. Power Sources 395, 271–279. https://doi.org/10.1016/j.jpowsour.2018.05.046.